AGU PUBLICATIONS

Geophysical Research Letters

RESEARCH LETTER
10.1002/2016GL070205

Key Points:
- A fault-bound valley involving Enterprise Rupes is linked to the Rembrandt basin on Mercury
- The valley could not have been formed simply by bounding fault scarps of opposite vergence
- Localization of the widely spaced thrust faults may be the result of long-wavelength buckling of Mercury's lithosphere

Supporting Information:
- Supporting Information S1

Correspondence to:
T. R. Watters,
watterst@si.edu

Citation:
Watters, T. R., L. G. J. Montési, J. Oberst, and F. Preusker (2016), Fault-bound valley associated with the Rembrandt basin on Mercury, *Geophys. Res. Lett.*, *43*, 11,536–11,544, doi:10.1002/2016GL070205.

Received 29 JUN 2016
Accepted 26 OCT 2016
Published online 16 NOV 2016

Fault-bound valley associated with the Rembrandt basin on Mercury

Thomas R. Watters[1], Laurent G. J. Montési[2], Jürgen Oberst[3,4], and Frank Preusker[3]

[1]Center for Earth and Planetary Studies, National Air and Space Museum, Smithsonian Institution, Washington, District of Columbia, USA, [2]Department of Geology, University of Maryland, College Park, Maryland, USA, [3]German Aerospace Center, Institute of Planetary Research, Berlin, Germany, [4]Extraterrestrial Laboratory, Moscow State University for Geodesy and Cartography (MIIGAiK), Moscow, Russia

Abstract The Rembrandt basin is crosscut by the largest fault scarp on Mercury, Enterprise Rupes, and a second scarp complex, Belgica Rupes, extends to the basin's rim. Topographic data derived from MESSENGER orbital stereo images show that these tectonic landforms bound a broad, relatively flat-floored valley with a mean width of ~400 km. Crosscutting relations suggest that the accumulation of structural relief likely postdates the formation and volcanic infilling of the Rembrandt basin. The valley floor, bound by fault scarps of opposite vergence, is significantly offset below the elevation of the back-scarp terrains. Along with an offset section of Rembrandt's rim, the elevation differences are evidence that the valley floor was lowered as a result of the formation of bounding fault scarps. The localization of the widely spaced thrust faults of Enterprise and Belgica Rupis and the offset of the valley floor may be the result of long-wavelength buckling of Mercury's lithosphere.

1. Introduction

The MErcury Surface, Space ENvironment, GEochemistry, and Ranging (MESSENGER) spacecraft made three flybys of Mercury before insertion into orbit in March 2011. Images obtained during the second flyby revealed a large, previously undetected basin, now named Rembrandt [*Watters et al.*, 2009a]. This basin is ~720 km in diameter, making it the fifth-largest well-defined [*Fassett et al.*, 2012], second-largest well-preserved, and one of the youngest impact basin on Mercury. Much of the main rim of the basin is topographically distinct, made up of rugged, inward facing scarps (Figure 1a).

Like the larger Caloris basin [*Murchie et al.*, 2008; *Watters et al.*, 2009b], the interior plains of Rembrandt have been deformed by a complex array of basin-radial and basin-concentric wrinkle ridges and graben (Figure 1b). In addition, the western rim and floor of Rembrandt are crosscut by the largest lobate scarp on Mercury [*Watters et al.*, 2009a; *Ruiz et al.*, 2012]. This large-scale thrust fault scarp, Enterprise Rupes, extends nearly 400 km across the basin floor, significantly offsetting the smooth plains material inside the basin as well as the floors and rims of two ~60 km diameter impact craters (Figure 1b).

Images obtained during MESSENGER's third flyby revealed a second large lobate scarp, Belgica Rupes, to the south that trends subparallel to Enterprise Rupes [*Watters et al.*, 2012; *Ruiz et al.*, 2012] (Figure 1c). Together, these scarps bound a broad valley or trough that extends from Rembrandt's southwestern rim. These widely spaced thrust fault scarps and other long-wavelength topographic features may provide insight into the large-scale deformation of Mercury's lithosphere.

2. Topography of the Basin, Trough, and Scarps

Orbital stereo images obtained from the Mercury Dual Imaging System (MDIS) [*Hawkins et al.*, 2007] wide-angle camera and narrow-angle camera have been used to generate a regional digital elevation model (DEM) [*Preusker et al.*, 2012]. The DEM was produced using stereo-photogrammetric processing involving block adjustment, multiimage matching, and surface point triangulation [*Gwinner et al.*, 2010; *Oberst et al.*, 2010; *Preusker et al.*, 2011]. The DEM of the Rembrandt region has a lateral spacing of 250 m/pixel and a vertical accuracy of about 30 m [*Preusker et al.*, 2012].

The major topographic features associated with the Rembrandt basin, the two large lobate scarps, and the broad intervening valley are clearly delineated in the DEM (Figure 2a). Within the Rembrandt

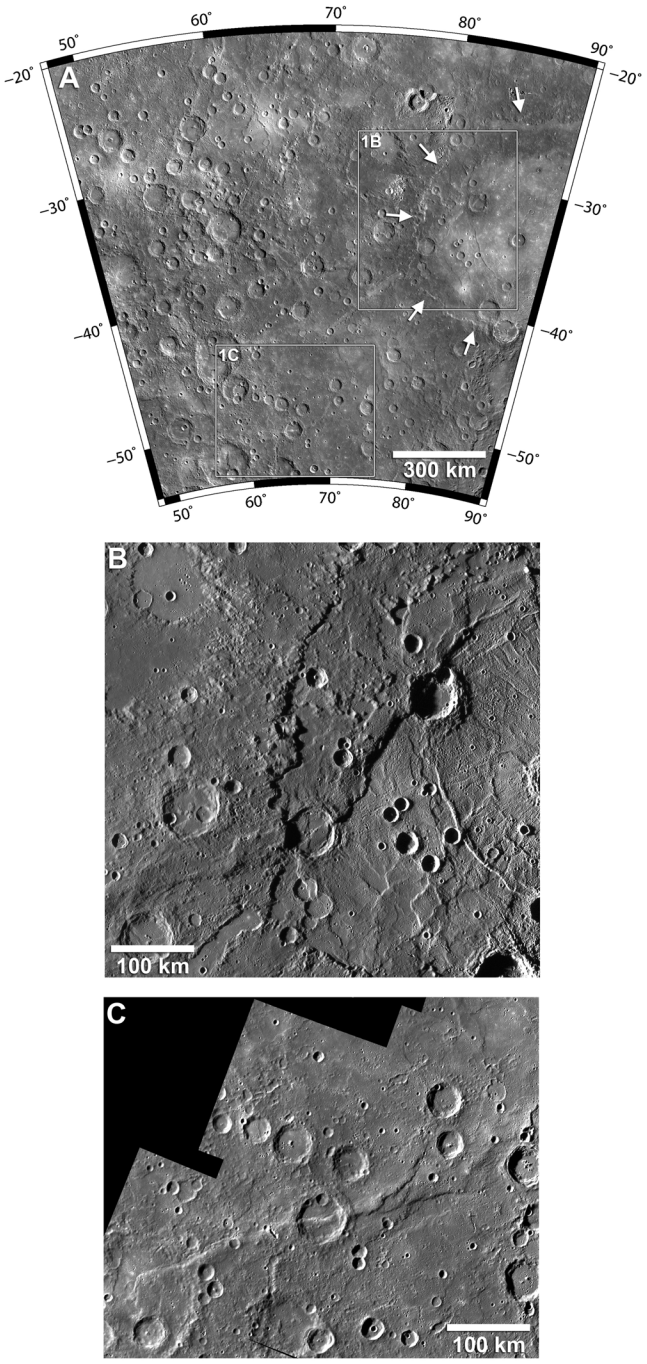

Figure 1. The Rembrandt basin and associated thrust fault scarps. (a) Monochrome mosaic of the Rembrandt basin area obtained by the MDIS cameras. The white boxes show the locations of Figures 1b and 1c. The white arrows show the location of the Rembrandt basin rim. (b) High incidence angle image mosaic of the large-scale lobate scarp Enterprise Rupes that cuts across the rim of the Rembrandt basin. The smooth plain material and the floors and rims of two ~60 km diameter impact craters within the basin are significantly offset by the thrust fault. Enterprise Rupes is located on the northern flank of the valley. (c) High incidence angle mosaic of Belgica Rupes, a lobate scarp to the south of Enterprise Rupes. Belgica Rupes is located on the southern flank of the trough.

basin the orientation of the crosscutting Enterprise Rupes changes to northeast-southwest, approximately tangential to an interior ring of wrinkle ridges (Figure 1b). This suggests that a buried basin interior ring that may underlie the wrinkle ridge ring influenced the orientation of the thrust fault [*Watters et al.*, 2009a].

The topographic data indicate that the offset of the basin floor across Enterprise Rupes is >2 km (Figure 2b). The slopes on the scarp face of Enterprise in the basin are >20° in some areas. The offset of the interior plains forms a wide bench-like feature that extends from the fault scarp to the rim (Figure 2a). The relief of the scarp and bench approaches the relief of the rim in some locations. The valley passes from the basin interior through the southwestern section of the basin rim and extends southwest for almost 1000 km (Figure 2a). The section of the rim in the valley is markedly lower than other sections, has isolated massifs, and displays a hummocky morphology unseen elsewhere along the rim.

Outside the basin, Enterprise Rupes forms the northern flank of the valley. The relief of Enterprise Rupes outside the basin reaches over 3 km measured from the valley floor (Figure 2c). This is the greatest relief of any measured lobate scarp on Mercury. Typical of large lobate scarps, Enterprise Rupes is asymmetric in cross section with a relatively steeply sloping scarp face and a more gently sloped back-scarp terrain that extends for almost 300 km (Figure 2c). Topographic profiles indicate that a single, primary thrust fault accounts for most of the structural relief of Enterprise Rupes with possible contributions to some of the relief in the back-scarp terrain from one or more secondary thrust faults. Enterprise Rupes also crosscuts a series of impact craters both within and outside of the Rembrandt basin [*Watters et al.*, 2009a; *Ruiz et al.*, 2012]

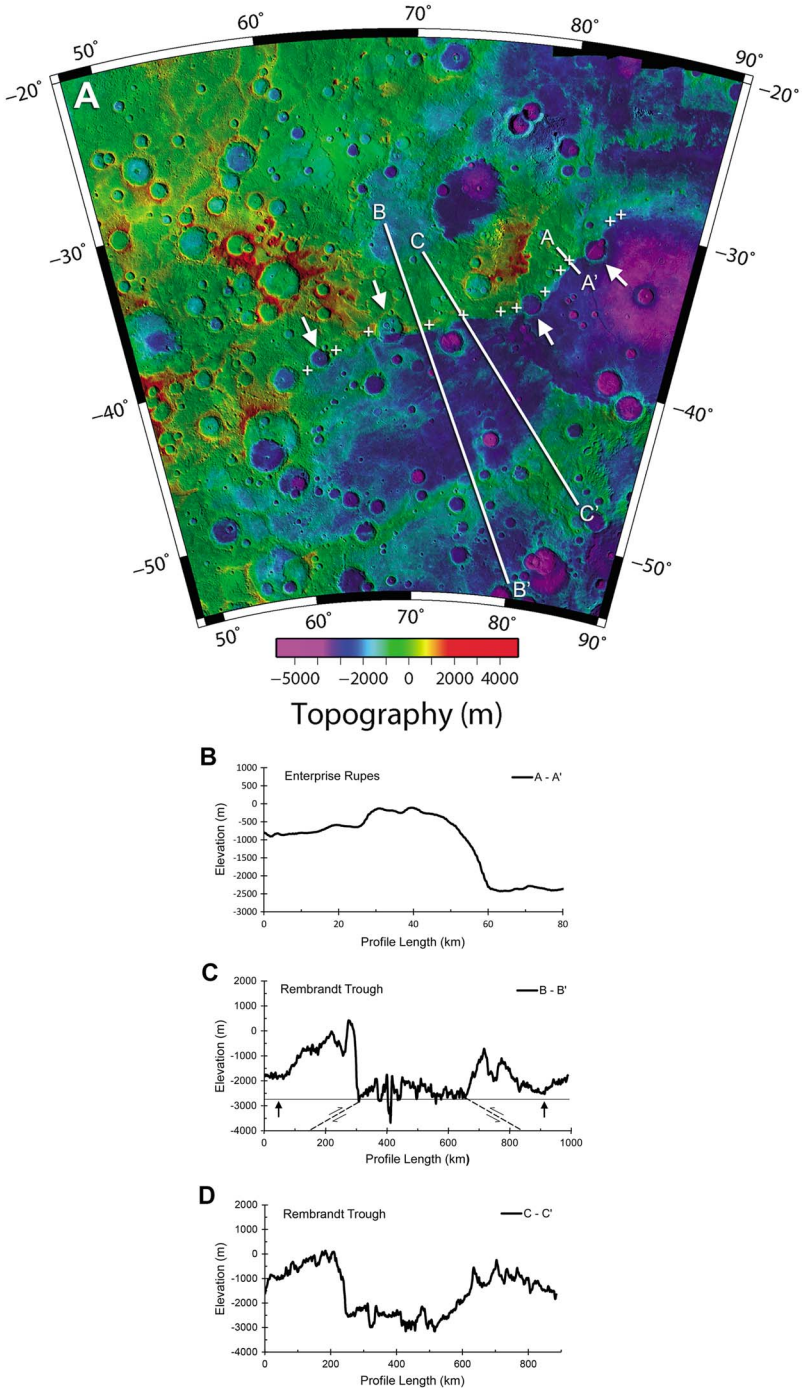

Figure 2. Topography of the fault scarps and valley. (a) Digital elevation model (DEM) derived from MDIS orbital stereo images. The rims of two ~60 km diameter impact craters within the basin (upward pointing white arrows) and an ~75 and ~60 km diameter craters outside the basin (downward pointing white arrows) are deformed by Enterprise Rupes. The white lines show the location of the profiles given in Figures 2b–2d. The crosses show the locations where the relief of Enterprise Rupes are measured and shown in Figure 3. Elevations are relative to a sphere of radius 2,440,000 m. (b) Topographic profile across Enterprise Rupes, where it crosscuts the floor of Rembrandt basin. The topographic profile was extracted from the DEM. (c) Topographic profile across the central portion of the fault-bound trough associated with the Rembrandt basin. The width of the trough at this location is ~440 km, and the relief on Enterprise Rupes exceeds 3 km. The black arrows indicate the locations of the back-scarp troughs and elevation offsets between them and the valley floor. The inferred locations of the thrust faults are shown by the thin dashed lines. (d) Topographic profile across the eastern portion of the fault-bound valley. The width of the trough at this location is ~260 km and is bound to the south by a broad, high-relief ridge-like landform with ~2 km of relief.

(Figure 2a). In addition to crosscutting the rim and floor of the Rembrandt basin and two ~60 km diameter impact craters within the basin (Figures 1b and 2a) [*Watters et al*., 2009a; *Ruiz et al*., 2012], Enterprise Rupes also cuts across a third that is ~75 km diameter about 350 km from the basin rim (Figure 2a). Beyond this crosscut crater to the southwest, the relatively steep, trough inward sloping (relative to the trough) scarp face becomes less distinct, but topographic data indicate that the structure continues to another ~60 km diameter impact crater. Although the rim and floor of this crater do not appear to be significantly offset, the topography shows that the crater is tilted, with its southern rim nearly 1000 m below its northern rim. The offset in elevation between the northern and southern rims and adjacent terrain is interpreted to be evidence that deformation related to Enterprise Rupes extends to and beyond this crater. The absence of an offset rim and floor suggests the transitions from a surface breaking to a blind thrust fault. Another ~75 km diameter crater about 30 km further to the southwest has little or no offset between its northern and southern rims, and thus, deformation related to the scarp appears to end at or near this crater (Figure 2a).

Image and topographic data show that the southern flank of the valley consists of a complex chain of contractional tectonic landforms. From the southwestern rim of Rembrandt for a distance of ~270 km, the southern flank is not defined by a clearly identifiable surface-breaking fault. Topographic data show that this section is bound by a broad, generally asymmetric ridge over 300 km wide with as much as ~2 km of relief (Figure 2d). Further to the west the broad ridge narrows and becomes more strongly asymmetric (Figure 2c). The lack of a clearly defined scarp in high incidence angle images suggests a fold or an underlying blind thrust fault. The morphology of the landform is consistent with a high-relief ridge, a structure closely related to lobate scarps [*Watters et al*., 2001, 2009a; *Ruiz et al*., 2012].

A narrowing high-relief ridge that becomes more asymmetric with an inward facing (relative to the trough) vergent side (Figure 2c) transitions into a complex series of lobate scarps, Belgica Rupes, that extends to the southwest for ~430 km (Figures 1c and 2a). The vergence of the series of scarps near the transition are outward facing, opposite from that of the high-relief ridge. To the southwest, the structure transitions back to a single inward facing scarp before crosscutting a ~60 km diameter impact crater (Figure 1c) and maintains the same sense of vergence along its remaining length. The orientation or the ridge-scarp complex is approximately parallel to Enterprise Rupes. The complex nature of the bounding contractional tectonic landforms, particularly Belgica Rupes [see *Ruiz et al*., 2012], may indicate an atypical tectonic setting related to the formation of the widely spaced faults and valley.

The width of the trough varies along its ~1000 km length (Figure 2a). The narrowest section of the trough is near the southwestern rim of the basin. Here the width (measured from peak-to-peak elevation across the trough) is ~280 km. Over a distance of ~250 km from the Rembrandt Basin's rim, the trough width increases to ~450 km (Figure 2c). The width reaches a maximum of ~470 km approximately midway along its length. Westward of this location, the trough narrows again and terminates diffusely in elevated, heavily cratered intercrater plains. The mean width, determined from six profiles spaced along the valley, is ~400 ± 70 km. Slopes on the bounding scarps and high-relief ridges are generally greater than 10° and locally exceed 20°, whereas slopes in the valley are generally less than 5°.

3. Timing of Deformation

Key constraints in determining the relative age of Enterprise Rupes and the fault bound valley are provided by the crosscutting relations with the Rembrandt rim and basin, impact craters, and smooth plains units interior and exterior to Rembrandt. The *N*(20) age of the Rembrandt basin, estimated by determining the number of craters with diameters 20 km or greater per million square kilometers, is 58 ± 16, indistinguishable from the *N* (20) value for the rim of the Caloris basin [*Watters et al*., 2009a]. The similarity in the crater size-frequency distribution for the rims of the Rembrandt and Caloris basins indicates that they are comparable in age. Smooth plains in the interior of Rembrandt, mapped on the basis of morphology and spectral characteristics, are interpreted to be volcanic in origin and are the oldest expanse of smooth plains on Mercury with an *N*(20) value of 45 ± 12 [*Denevi et al*., 2013]. *Ferrari et al*. [2014] estimated ages for Rembrandt (~3.8 Ga) and the interior smooth plains (~3.6 Ga) using a model production function method, comparable to previous estimates [*Watters et al*., 2009a; *Fassett et al*., 2012; *Denevi et al*., 2013].

The crosscut and offset rim and floor materials of the Rembrandt basin are clear evidence of postbasin formation slip on thrust fault segments of Enterprise Rupes. This and crosscut impact craters suggest that

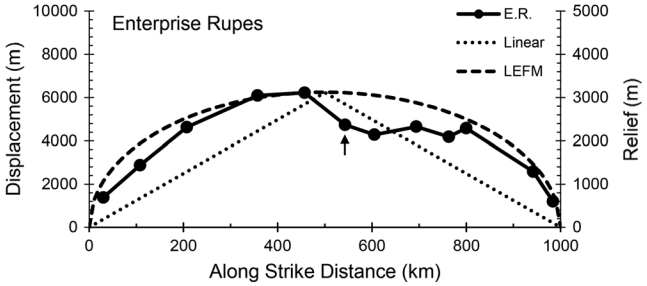

Figure 3. Relief and displacement profiles of the Enterprise Rupes thrust fault. The relief was measured at 12 locations along Enterprise Rupes both outside and within Rembrandt basin. The displacement on the thrust fault was estimated from the relief (h) assuming a planar fault geometry, where the displacement (D) necessary to restore the topography is $D = h/sin\theta$ for a fault plane dip θ of 30°. The two dashed lines show the model displacement profiles, a idealized linear displacement profile (short dashes), and a simple LEFM displacement model (long dashes) [see *Cowie and Scholz*, 1992; *Schultz et al*., 2010]. The black arrow indicates the location of the rim of Rembrandt basin. Elevations are relative to a sphere of radius 2,440,000 m.

Enterprise Rupes postdates the formation and infilling of the Rembrandt basin [*Watters et al*., 2009a]. The relatively low elevation of the southwestern portion of Rembrandt's rim also suggests post-basin formation tectonic modification of the basin (Figure 2a). Belgica Rupes and the high-relief ridge that form the southern boundary of the valley associated with Rembrandt do not exhibit crosscutting relations with the rim and floor of the basin. However, Belgica Rupes clearly crosscuts an ~60 km diameter impact crater, with a comparable degradation state to the ~60 km diameter craters within Rembrandt basin crosscut by Enterprise Rupes. This suggest that Enterprise Rupes and Belgica Rupes are cogenetic, consistent with evidence that thrust faulting was broadly distributed over a long portion of Mercury's geologic history [*Banks et al*., 2015].

Ferrari et al. [2014] speculated that the formation of Enterprise Rupes predates the formation of the Rembrandt basin. They suggested that postscarp formation of the basin perturbed the stress field and reoriented the strike of a branch of the fault as it grew within the new basin. Although a prebasin initiation of thrust faulting cannot be completely ruled out, there are several lines of evidence that suggest otherwise. First, there is no evidence of reactivation of a now basin-interior preexisting thrust fault with the orientation of Enterprise Rupes outside the basin (Figure 1b). Second, as noted by *Watters et al*. [2009a], the basin-interior northeast-southwest oriented segment of Enterprise is approximately tangential to an interior ring of wrinkle ridges, suggesting that the thrust fault was influenced by a buried basin interior ring structure, also possibly expressed by a corresponding, roughly circular topographic low in the center of the basin (Figure 2a). Third, the formation of the Rembrandt basin is expected to have resulted in significant impact damage to crustal materials within and outside the basin and likely significantly altered or reset the preexisting stress field within the damage zone [see *Freed et al*., 2009]. Thus, if slip on the Enterprise Rupes thrust fault initiated prior to the formation of the Rembrandt basin, the growth of the fault segment in the basin interior would be expected to have been interrupted until compressional stress levels recovered and fault slip was reestablished.

The interruption of fault growth on the interior segment or the development of a new interior fault segment might be expressed in the distribution of relief and inferred displacement along the fault. The relief of Enterprise Rupes measured at 12 locations along strike, both inside and outside the basin, reaches a maximum (~3.2 km) at about the midpoint of the structure (~460 km along its length; Figure 3), where the maximum inferred displacement is >6 km (assuming a fault plane with a dip of 30°). This corresponds to a displacement D to fault length L ratio γ of ~6.6×10^{-3}, consistent with other large-scale lobate thrust fault scarps on Mercury [*Watters et al*., 2013] and on Mars, but is almost an order of magnitude smaller than the γ of terrestrial foreland thrust belt faults and the Wind River thrust fault [see *Watters*, 2003]. The displacement profile is in good agreement with the elliptical profile predicted by a simple linear elastic fracture mechanic (LEFM) model, suggesting that much of the accumulated fault growth occurred along the length of a single fault [see *Cowie and Scholz*, 1992; *Schultz et al*., 2010]. Although the relief and corresponding displacement decreases somewhat near the basin margin, it does not drop below 2 km. A large decrease in the displacement at this location would be expected if Enterprise Rupes developed by relatively recent linkage of basin-exterior and basin-interior fault segments that grew independently over a long period of time. Likewise, the fault segment inside Rembrandt has >2 km of relief along half of its length before dropping below 2 km near its northeastern terminus (Figure 3). The flattened portion of the displacement profile

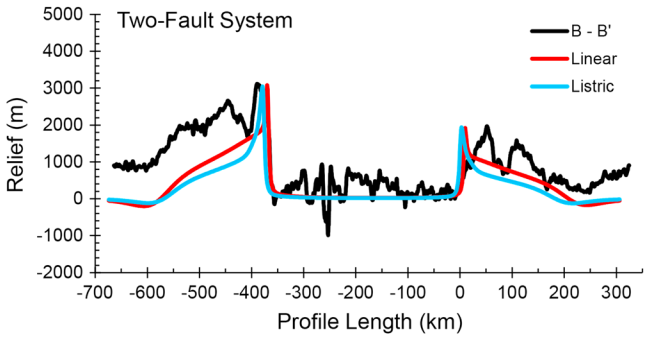

Figure 4. Elastic dislocation model of opposite facing thrust faults. The models show that two opposing thrust faults are insufficient to explain the observed topography, specifically the observed offsets between the valley floor and the back-scarp troughs. The vertical displacement above propagating faults is modeled using the elastic dislocation program COULOMB (details in the supporting information) [*Okada*, 1992; *Stein et al*., 1994; *Lin and Stein*, 2005; *Toda et al*., 2005]. The linear fault geometry is approximated by a single fault plane with a dip of 15° [see *Watters et al*., 2002]. The listric geometry is approximated by fault segments with fault plane dip angles θ of 40°, 30°, 20°, and 15° [see *Watters*, 2004]. The final fault segment in both models flattens into a décollement at a maximum depth T of 60 km (see supporting information). The amount of slip D on the fault segments was chosen to approximate the maximum relief of Enterprise Rupes and the Belgica Rupes high-relief ridge.

corresponds to the broad, interior bench (see above) and may reflect a contrast in the mechanical properties between the basin-interior materials and the exterior intercrater plains or the influence of a buried interior ring structure (Figure 3). If a fault segment boundary is located at the rim of the basin, its identification is complicated by the presence of a 60 km diameter crosscut crater (Figure 1b) with a floor offset of ~1.1 km and a tilted rim (southeastern rim is ~1.7 km below the northwestern rim). If Enterprise Rupes did develop by growth of two fault segments, the faults likely linked relatively early and a preexisting basin rim may have influenced the location where an interior and exterior segment merged. Together these observations argue against formation or appreciable growth on the Enterprise Rupes thrust fault before the formation of the Rembrandt basin. Furthermore, crosscutting relations with small impact craters, <3 km in diameter that are likely Kuiperian in age (<~1.0 Ga), suggest the Enterprise Rupes thrust fault has been active over a large portion of the Mercury's recorded geologic history [*Banks et al*., 2015].

4. Interpretation and Discussion

The image and topographic data indicate that the valley associated with the Rembrandt basin is bound by thrust fault scarps with opposite vergence along much of its length (Figures 2a and 2c). In particular, elevation offsets between the valley floor and back-scarp troughs (Figure 2c) are predicted by elastic dislocation models of fault slip [*Watters et al*., 2002]. The valley floor–back-scarp trough offset is up to ~400 m on the southern scarp and up to ~1000 m on Enterprise Rupes (Figure 2c). Simple two-fault elastic dislocation models involving opposite facing, thrust faults that extend to a depth of 60 km and flatten into a décollement at the brittle-ductile transition (see supporting information) predict shallow back-scarp troughs that are below the elevation of the valley floor (Figure 4), inconsistent with the observed topography. The topographically lower portion of the basin rim in the valley relative to other sections of Rembrandt's rim (see above) and the observed offsets of valley floor–back-scarp troughs may be evidence that the valley floor was lowered as a result of the formation of bounding fault scarps. The association of the valley and the contractional tectonic landforms (lobate scarps and high-relief ridges) suggests that the valley and bounding structures may have been localized by a long-wavelength, lithospheric-scale mechanism. One such mechanism is buckling of the lithosphere, a mechanism proposed to accommodate a fraction of the horizontal contraction on Mercury [*Dombard et al*., 2001]. However, the magnitude of stress needed to explain the generation the lobate fault scarps that bound the valley discussed here would need to exceed the values envisioned by *Dombard et al.* [2001], which lead only to buckling. With an average slip of 4 km and assuming a dip of 30°, each structure accommodated ~3.5 km of shortening, corresponding to ~1.5% strain over the width of the valley.

Although the structures that bound the valley discussed here are far apart, they may still be cogenetic, as coherent structures of even longer wavelength have been observed on Mercury. For example, Mercury Laser Altimeter and stereo-derived topography [*Oberst et al*., 2010; *Solomon et al*., 2012; *Zuber et al*., 2012] revealed long-wavelength topographic undulation that appear to postdate the emplacement of the smooth plains in the northern high latitudes and in the Caloris basin [*Head et al*., 2011; *Zuber et al*., 2012] and likely also postdate subsequent deformation of the smooth plains [*Klimczak et al*., 2013]. The scale of the

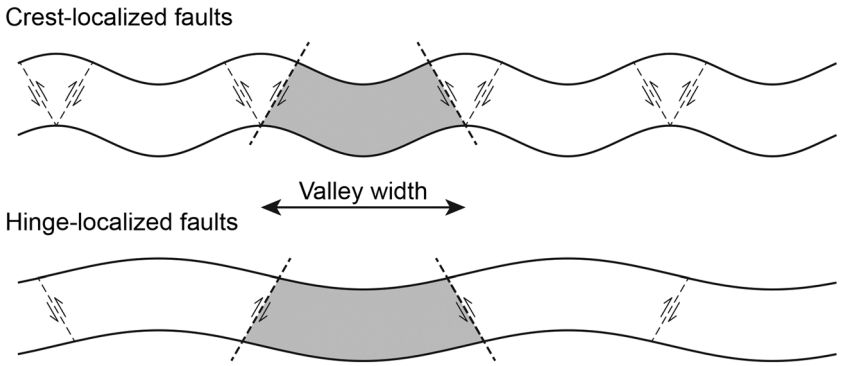

Figure 5. Fold-crest localized faulting versus fold-hinge localized faulting. In the case of fold-crest localized faulting, thrust faults bound a trough or valley, where the valley width is approximately equal to the buckling wavelength. In the case of fold-hinge localized faulting, the thrust fault-bound valley width is approximately one half the buckling wavelength [*Gerbault et al*., 1999].

topographic undulations that effect the interior smooth plains of Caloris are much greater than the width of the fault bound valley associated with Rembrandt, with wavelengths of up to 1300 km and amplitudes up to 3 km [*Klimczak et al*., 2013]. Wavelengths of this scale far exceed those expected from lithospheric buckling given the current estimates of Mercury's interior structure. These long-wavelength topographic undulations are associated with positive gravity anomalies and may be supported by deep-seated dynamic flow [*James et al*., 2015].

Faulting is expected to develop when folds reach sufficient amplitude for a brittle yield criterion to be satisfied. Thrust faults may first appear at the crest of folds, propagating upward from the base of the plate (where horizontal stress is maximized; Figure 5). In this case, fold crests correspond to the change of elevation between the trough floor and surrounding regions and the instability wavelength is similar to the width of the trough or about 400 km. Alternatively, failure may occur at the hinge of folds (where the shear stress is maximized) [*Lambeck*, 1983; *Gerbault et al*., 1999]. In this case, the implied fold wavelength is twice the valley width or about 800 km (Figure 5). The fold amplitude must be small to preserve the generally uniform, relatively low elevation of the valley. Buckling instability theory links fold wavelength to the mechanical properties of the lithosphere at the time of deformation [*Zuber and Aist*, 1990; *Watters*, 1991; *Dombard et al*., 2001]. Regularly spaced faults can also develop from localization instability, where faults interact with the rheological stratification of the lithosphere, especially the transition from brittle to ductile behavior [*Montési and Zuber*, 2003]. In that model, the valley floor remains undeformed.

Modeling of the depth of faulting of large-scale lobate scarp thrust faults and analysis of dynamic localization mechanisms suggest that the lithosphere behaved brittlely to ~30–60 km depth at the time of thrust faulting [*Watters et al*., 2002; *Nimmo and Watters*, 2004; *Zuber et al*., 2010]. This range of lithosphere thickness corresponds to a buckling wavelength to lithospheric thickness ratio of ~5–10 if the wavelength is ~400 km, consistent with buckling instability models [*Zuber and Aist*, 1990; *Watters*, 1991; *Montési and Zuber*, 2003]. If the wavelength is ~800 km, the ratio is between ~10 and 25, which is at the high end of the ratios predicted by buckling instability models [*Zuber and Aist*, 1990; *Watters*, 1991; *Montési and Zuber*, 2003]. A typical range of instability wavelength of 2 to 10 times the buckling wavelength implies that the brittle-ductile transition would be 80 to 400 km depth for a wavelength of 800 km and 40 to 200 km depth for a wavelength of 400 km. Interestingly, the upper estimate above is similar to the thickness of the outer solid layer of the planet, as deduced from moment of inertia and libration amplitude [*Smith et al*., 2012; *Hauck et al*., 2013; *Mazarico et al*., 2014; *Verma and Margot*, 2016]. In either case, a thick brittle layer would be consistent with formation of the wide valley discussed here late in Mercury's history. It is even possible that the brittle layer in present-day Mercury is not limited by the thermal structure of its mantle but by the compositional contrast between the mantle, which would be fully brittle, and the subjacent core. Understanding the mechanical structure of the lithosphere and mantle provides important constraints on buckling and localization instability models that may account for long-wavelength, low-amplitude folding of the lithosphere and the localization of widely spaced thrust faults.

Acknowledgments

We thank the anonymous reviewers for their helpful comments and suggestions that greatly improved the manuscript. We also thank S.C. Solomon and S.A. Hauck, II for their helpful suggestions on an early manuscript. J. Oberst gratefully acknowledges being hosted by MIIGAiK and supported by the Russian Science Foundation under project 14-22-00197. We are grateful to the MESSENGER engineers and technical support personnel at the Johns Hopkins University Applied Physics Laboratory. This work is also supported by NASA grant NNX07AR60G. Data used to produce the results of this paper can be obtained upon request from the first author. MESSENGER images are available from the Planetary Data System Cartography and Imaging Sciences Node (http://pds-imaging.jpl.nasa.gov/schedules/mess_release.html).

References

Banks, M. E., Z. Xiao, T. R. Watters, R. G. Strom, S. E. Braden, C. R. Chapman, S. C. Solomon, C. Klimczak, and P. K. Byrne (2015), Duration of activity on lobate-scarp thrust faults on Mercury, *J. Geophys. Res. Planets*, *120*, 1751–1762, doi:10.1002/2015JE004828.

Cowie, P. A., and C. H. Scholz (1992), Physical explanation for the displacement-length relationship of faults using a post-yield fracture mechanics model, *J. Struct. Geol.*, *14*, 1133–1148.

Denevi, B. W., et al. (2013), The distribution and origin of smooth plains on Mercury, *J. Geophys. Res Planets.*, *118*, 891–907, doi:10.1002/jgre.20075.

Dombard, A. J., S. A. Hauck, S. C. Solomon, and R. J. Phillips (2001), Potential for long wavelength folding on Mercury, *Proc. Lunar Planet. Sci.*, *32*, Abstract 2035.

Fassett, C. I., et al. (2012), Large impact basins on Mercury: Global distribution, characteristics, and modification history from MESSENGER orbital data, *J. Geophys. Res.*, *117*, E00L08, doi:10.1029/2012JE004154.

Ferrari, S., M. Massironi, S. Marchi, P. K. Byrne, C. Klimczak, E. Martellato, and G. Cremonese (2014), Age relations of the Rembrandt basin and Enterprise Rupes, Mercury, *Geol. Soc., London, Spec. Pub.*, doi:10.1144/SP401.20.

Freed, A. M., S. C. Solomon, T. R. Watters, R. J. Phillips, and M. T. Zuber (2009), Could Pantheon Fossae be the result of the Apollodorus crater-forming impact within the Caloris basin, Mercury?, *Earth Planet. Sci. Lett.*, *285*, 320–327.

Gerbault, M., E. B. Burov, A. N. B. Poliakov, and M. Daignières (1999), Do faults trigger folding in the lithosphere?, *Geophys. Res. Lett.*, *26*, 271–274, doi:10.1029/1998GL900293.

Gwinner, K., et al. (2010), Topography of Mars from global mapping by HRSC high-resolution digital terrain models and orthoimages: Characteristics and performance, *Earth Planet. Sci. Lett.*, *294*, 506–519.

Hauck, S. A., II, et al. (2013), The curious case of Mercury's internal structure, *J. Geophys. Res. Planets*, *118*, 1204–1220, doi:10.1002/jgre.20091.

Hawkins, S. E., III, et al. (2007), The Mercury dual imaging system on the MESSENGER spacecraft, *Space Sci. Rev.*, *131*, 247–338, doi:10.1007/s11214-007-9266-3.

Head, J. W., et al. (2011), Flood volcanism in the northern high latitudes of Mercury revealed by MESSENGER, *Science*, *333*, 1853–1856.

James, P. B., M. T. Zuber, R. J. Phillips, and S. C. Solomon (2015), Support of long-wavelength topography on Mercury inferred from MESSENGER measurements of gravity and topography, *J. Geophys. Res. Planets*, *120*, 287–310, doi:10.1002/2014JE004713.

Klimczak, C., C. M. Ernst, P. K. Byrne, S. C. Solomon, T. R. Watters, S. L. Murchie, F. Preusker, and J. A. Balcerski (2013), Insights into the subsurface structure of the Caloris basin, Mercury, from assessments of mechanical layering and changes in long-wavelength topography, *J. Geophys. Res. Planets*, *118*, 2030–2044, doi:10.1002/jgre.20157.

Lambeck, K. (1983), Structure and evolution of the intracratonic basis of central Australia, *Geophys. J. R. Astron. Soc.*, *74*, 843–886.

Lin, J., and R. S. Stein (2005), Stress triggering in thrust and subduction earthquakes, and stress interaction between the southern San Andreas and nearby thrust and strike-slip faults, *J. Geophys. Res.*, *109*, B02303, doi:10.1029/2003JB002607.

Mazarico, E., A. Genova, S. Goossens, F. G. Lemoine, G. A. Neumann, M. T. Zuber, D. E. Smith, and S. C. Solomon (2014), The gravity field, orientation, and ephemeris of Mercury from MESSENGER observations after three years in orbit, *J. Geophys. Res. Planets*, *119*, 2417–2436, doi:10.1002/2014JE004675.

Montési, L. G. J., and M. T. Zuber (2003), Spacing of faults at the scale of the lithosphere and localization instability: 1. Theory, *J. Geophys. Res.*, *108*(B2), 2110, doi:10.1029/2002JB001923.

Murchie, S. L., et al. (2008), Geology of the Caloris basin, Mercury: A new view from MESSENGER, *Science*, *321*, 73–76.

Nimmo, F., and T. R. Watters (2004), Depth of faulting on Mercury: Implications for heat flux and crustal and effective elastic thickness, *Geophys. Res. Lett.*, *31*, L02701, doi:10.1029/2003GL018847.

Oberst, J., F. Preusker, R. J. Phillips, T. R. Watters, J. W. Head, M. T. Zuber, and S. C. Solomon (2010), The morphology of Mercury's Caloris basin as seen in MESSENGER stereo topographic models, *Icarus*, *209*, 230–238.

Okada, Y. (1992), Internal deformation due to shear and tensile faults in a half-space, *Bull. Seism. Soc. Am.*, *82*, 1018–1040.

Preusker, F., J. Oberst, J. W. Head, T. R. Watters, M. S. Robinson, M. T. Zuber, and S. C. Solomon (2011), Stereo topographic models of Mercury after three MESSENGER flybys, *Planet. Space Sci.*, *59*, 1910–1917.

Preusker, F., et al. (2012), Togography of Mercury from stereo images: First samples from MESSENGER orbital mapping, *Lunar Planet. Sci.*, *43*, Abstract 1913.

Ruiz, J., V. López, J. M. Dohm, and C. Fernández (2012), Structural control of scarps in the Rembrandt region of Mercury, *Icarus*, *219*, 511–514.

Schultz, R. A., R. Soliva, C. H. Okubo, and D. Mege (2010), Fault populations, in *Planetary Tectonics*, edited by T. R. Watters and R. A. Schultz, pp. 457–510, Cambridge Univ. Press, Cambridge.

Smith, D. E., et al. (2012), Gravity field and internal structure of Mercury from MESSENGER, *Science*, *336*, 212–216.

Solomon, S. C., et al. (2012), Long-wavelength topographic change on Mercury: Evidence and mechanisms, *Proc. Lunar Planet. Sci.*, *43*, Abstract 1578.

Stein, R. S., G. C. P. King, and J. Lin (1994), Stress triggering of the 1994 $M = 6.7$ Northridge California, earthquake by its predecessors, *Science*, *265*, 1432–1435.

Toda, S., R. S. Stein, K. Richards-Dinger, and S. Bozkurt (2005), Forecasting the evolution of seismicity in Southern California: Animations built on earthquake stress transfer, *J. Geophys. Res.*, *110*, B05S16, doi:10.1029/2004JB003415.

Verma, A. K., and J.-L. Margot (2016), Mercury's gravity, tides, and spin from MESSENGER radio science data, *J. Geophys. Res. Planets*, *121*, 1627–1640, doi:10.1002/2016JE005037.

Watters, T. R. (1991), Origin of periodically spaced wrinkle ridges on the Tharsis plateau of Mars, *J. Geophys. Res.*, *96*, 15,599–15,616, doi:10.1029/91JE01402.

Watters, T. R. (2003), Thrust faulting along the dichotomy boundary in the eastern hemisphere of Mars, *J. Geophys. Res.*, *108*(E6), 5055, doi:10.1029/2002JE001934.

Watters, T. R. (2004), Elastic dislocation modeling of wrinkle ridges on Mars, *Icarus*, *171*, 284–294.

Watters, T. R., M. S. Robinson, and A. C. Cook (2001), Large-scale lobate scarps in the southern hemisphere of Mercury, *Mercury Special Issue-Planet. Space Sci.*, *49*(14–15), 1523–1530.

Watters, T. R., R. A. Schultz, M. S. Robinson, and A. C. Cook (2002), The mechanical and thermal structure of Mercury's early lithosphere, *Geophys. Res. Lett.*, *29*(11), 37–1–37-4, doi:10.1029/2001GL014308.

Watters, T. R., J. W. Head, S. C. Solomon, M. S. Robinson, C. R. Chapman, B. W. Denevi, C. I. Fassett, S. L. Murchie, and R. G. Strom (2009a), Evolution of the Rembrandt impact basin on Mercury, *Science*, *324*, 618–621.

Watters, T. R., S. L. Murchie, M. S. Robinson, S. C. Solomon, B. W. Denevi, S. L. André, and J. W. Head (2009b), Emplacement and tectonic deformation of smooth plains in the Caloris basin, Mercury, *Earth Planet. Sci. Lett.*, *285*, 309–319.

Watters, T. R., et al. (2012), Tectonic features on Mercury: An orbital view with MESSENGER, *Proc. Lunar Planet. Sci.*, *43*, Abstract 2121.
Watters, T. R., et al. (2013), Distribution of prominent lobate scarps on Mercury: Contribution to global radial contraction, *Lunar Planet. Sci.*, *44*, Abstract 2213.
Zuber, M. T., and L. L. Aist (1990), The shallow structure of the Martian lithosphere in the vicinity of the ridged plains, *J. Geophys. Res.*, *95*, 14,215–14,230, doi:10.1029/JB095iB09p14215.
Zuber, M. T., et al. (2010), Accommodation of lithospheric shortening on Mercury from altimetric profiles of ridges and lobate scarps measured during MESSENGER flybys 1 and 2, *Icarus*, *209*, 247–255.
Zuber, M. T., et al. (2012), Topography of the northern hemisphere of Mercury from MESSENGER laser altimetry, *Science*, *336*, 217–220.